Geochemical Perspectives Letters

SHRIMP 4-S isotope systematics of two pyrite generations in the 3.49 Ga Dresser Formation

L. Liu[1*], T.R. Ireland[1], P. Holden[1]

OPEN ACCESS

doi: 10.7185/geochemlet.2113

Abstract

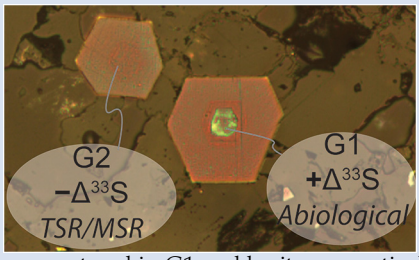

The 3.49 Ga Dresser Formation has been considered to host evidence of the earliest microbes metabolising sulfur species on Earth. However, previous bulk analyses and *in situ* measurements conclude disparate metabolisms based on opposite $\Delta^{33}S$[1]. This study first established the generations of pyrite growth, and then measured the multiple sulfur isotopes *in situ* using Sensitive High Resolution Ion MicroProbe-Stable Isotope analyses. Two main generations of pyrite were revealed based on core-rim textures and multiple sulfur isotopic compositions: $\Delta^{33}S$-positive Generation One (G1) and $\delta^{34}S$- and $\Delta^{33}S$-negative Generation Two (G2). In the chert-barite unit, the diluted $\Delta^{33}S$-positive and $\Delta^{33}S$-negative photochemical products were mainly sequestered in G1 and barite, respectively. G2 were formed *via* the sulfide pathway with sulfur derived from sulfate reduction and magmatic H_2S. The $\delta^{34}S$-$\Delta^{33}S$-$\Delta^{36}S$[1] systematics suggests an abiological origin for G1, and thermochemical and possible (minor) microbial sulfate reduction for G2.

Received 8 September 2020 | Accepted 19 March 2021 | Published 10 May 2021

Introduction

The 3.49 Ga Dresser Formation in the Pilbara Craton, Western Australia has been widely considered to preserve palaeontological and geochemical evidence of Earth's earliest life (*e.g.*, Buick *et al.*, 1981; Ueno *et al.*, 2006; Shen *et al.*, 2009; Noffke *et al.*, 2013). The multiple sulfur isotopes of sulfate and sulfide in the Dresser Formation have been measured by both bulk and *in situ* analytical methods. Results of bulk methods support microbial sulfate reduction (MSR; Ueno *et al.*, 2008; Shen *et al.*, 2009) while *in situ* measurements support elemental sulfur disproportionation (Philippot *et al.*, 2007). The differences in these data sets are profound. Although recent *in situ* studies have confirmed separately the $\delta^{34}S$–$\Delta^{33}S$ positively correlated $\Delta^{33}S$-negative (Baumgartner *et al.*, 2020) and $\Delta^{33}S$-positive (Wacey *et al.*, 2015) pyrites, the relationship between the two groups remains unknown.

The chert-barite unit of Dresser Formation was generated by a complex hydrothermal system, thus the pyrites are likely to preserve multiple generations resulting from multiple stages of hydrothermal events (Van Kranendonk *et al.*, 2008). This study established the generations of pyrite formation, and then measured the multiple sulfur isotopes *in situ*. We exploited the *in situ* capabilities of SHRIMP-SI allowing ^{36}S measurements in pyrite with a precision at a similar level to conventional bulk methods. In this way, we uniquely identified the sulfur isotopic composition of each generation of pyrites, and provided constraints on their formation pathways.

Geological Setting

The 3.49 Ga (Tessalina *et al.*, 2010) Dresser Formation crops out as a ring of the North Pole Dome in the Pilbara Craton. It consists of metabasalt interlayered with three chert horizons (Ueno *et al.*, 2008). The lowermost chert hosts abundant barite, referred to as the chert-barite unit, and is composed of chert, barite, carbonate, sandstone and conglomerate. Below this unit are thousands of silica ± sulfides (pyrite and sphalerite) ± organic matter veins and barite veins intruding and transecting the underlying komatiitic basalt. The chert-barite unit and the veins are generally considered to be formed in a volcanic caldera, with sedimentation accompanied by volcanism, hydrothermal circulation and precipitation, and tectonic activity (Van Kranendonk *et al.*, 2008). The hydrothermal fluids ascended along growth faults and deposited as concordant layers in a feeder-deposit manner. Detailed geological setting is in Supplementary Information (SI).

Samples and Methods

The investigated samples are from two drill cores: PDP2b and PDP2c. Detailed sample descriptions are in Table S-1. The drill core sections were made into polished mounts, which were immersed in sodium hypochlorite solution (8–12.5 % NaOCl) to reveal the internal textures of pyrites. The principle of pyrite etching is in SI. Appropriate pyrites were selected for subsequent BSE (Back Scattered Electron) imaging, EDS (Energy Dispersive X-ray Spectroscopy) and Raman spectroscopy analyses. Then

1. Research School of Earth Sciences, The Australian National University, Canberra ACT 2601, Australia
* Corresponding author (email: emmaliu1016@gmail.com)

[1] $\Delta^{33}S$ and $\Delta^{36}S$ quantify the magnitudes of sulfur mass-independent fractionations (S-MIFs) during a reaction, which are the deviations of the $^{34}S/^{32}S$, $^{33}S/^{32}S$, and $^{36}S/^{32}S$ isotopic ratios from those expected solely based on their mass differences (see section 3.2 in the Supplementary Information).

the pyrites were measured for multiple sulfur isotopes using SHRIMP-SI. Detailed methods are in SI.

Results

Pyrites occur as tiny grains aligned in an array within barite (Py-i), pyrite laminae (Py-ii), individual grains (IG) or clusters associated with silica veinlets/beads in barite (within veinlet, Py-iii; on the wall of veinlet, Py-iv; adjacent to both barite and chert, Py-v), IG in barite with silica veinlets/beads (Py-vi), IG in chert with barite crystal fans (Py-vii), and IG in silica-barite-carbonate veins in hydrothermally altered komatiitic basalt (Py-viii) (Fig. S-2). Some pyrites show core-rim textures (portions of Py-i to vi and Py-viii) while the others are homogeneous (Figs. 1, S-3). The sulfur isotopic composition exhibits evident dependence on the internal texture and petrography of pyrite. The cores show a tendency towards positive $\delta^{34}S$ and $\Delta^{33}S$, whereas the rims have more negative $\delta^{34}S$ and $\Delta^{33}S$ (Fig. S-8). Py-ii are mostly core-rim textured and display both negative and positive $\delta^{34}S$, $\Delta^{33}S$ and $\Delta^{36}S$, whereas Py-iii to vi are characterised by negative $\delta^{34}S$ and $\Delta^{33}S$ and positive $\Delta^{36}S$, with only a few exceptions. Py-vii show characteristic positive $\delta^{34}S$ and $\Delta^{33}S$, and Py-viii exhibit negative $\Delta^{33}S$ and positive $\delta^{34}S$ (Table 1, Fig. S-9). Detailed petrography, internal texture, and sulfur isotopic compositions are in SI.

Discussion

The core-rim relationship combined with sulfur isotopic composition reveals two main generations ($\Delta^{33}S$-positive, euhedral to subhedral, locally porous G1 and $\Delta^{33}S$-negative, anhedral G2) in the core-rim textured pyrites. The majority have $\Delta^{33}S$-positive cores and $\Delta^{33}S$-negative rims, indicating that $\Delta^{33}S$-positive precede $\Delta^{33}S$-negative pyrites. $\Delta^{33}S$-0 (close to 0, considering uncertainties) pyrites are widespread, and can be formed *via* the sulfide pathway ($Fe^{2+} + S^{2-} = [FeS]$, $[FeS] + H_2S = FeS_2 + H_2$; Rickard and Luther, 1997) with magmatic H_2S abundant in the Dresser hydrothermal system throughout the multiple stages of hydrothermal events (Ueno *et al.*, 2008 and references therein). $\Delta^{33}S$-0 pyrites can be synchronous with $\Delta^{33}S$-positive and $\Delta^{33}S$-negative pyrites, because both $\Delta^{33}S$-positive and $\Delta^{33}S$-negative pyrites show evident positive correlations between $\delta^{34}S$ and $\Delta^{33}S$ (Fig. 2b), indicating two separate mixing trends between two respective end members, with one being $\Delta^{33}S$-0. Minor pyrites show $\Delta^{33}S$-negative cores and rims, suggesting two stages of G2.

Some Py-ii show two additional growth zones prior to G1 and G2 (Fig. 2a). The earlier zones (G1′) are tiny porous grains, the $\Delta^{33}S$ of which is beyond the resolution ability of SHRIMP spots. However, the textures of these pyrites are similar to the cores of core-rim textured Py-i (Fig. 1a) that have been shown to be $\Delta^{33}S$-positive (Philippot *et al.*, 2007). The later zones

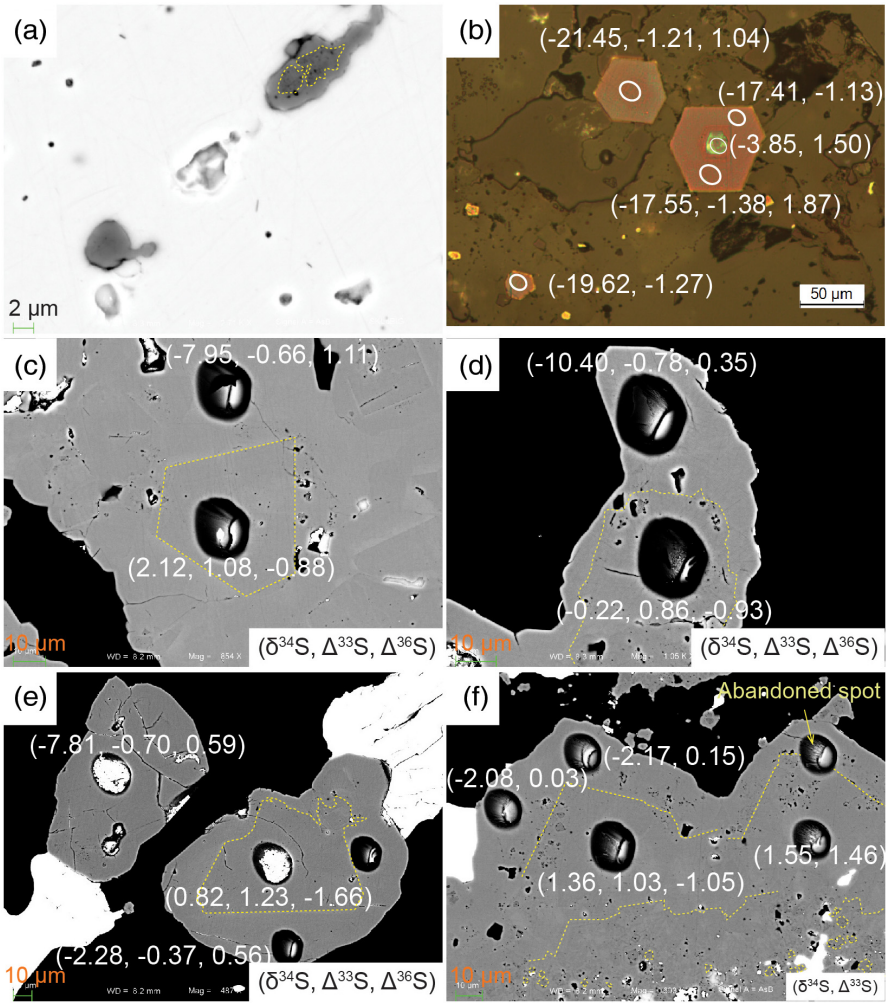

Figure 1 **(a)** BSE image of tiny pyrites aligned in an array within barite. **(b)** Photomicrograph (reflected light, NaOCl-etched pyrite) and **(c–f)** BSE images of core-rim textured pyrites. **(a, c–f)** are from PDP2c_97.17–97.20 m; **(b)** is from PDP2b_90.94–90.97 m.

Table 1 Classification and quadruple S isotopic compositions of pyrites.

Pyrite type	Description	$\delta^{34}S$ (‰)	$\Delta^{33}S$ (‰)	$\Delta^{36}S$ (‰)
Py-i	Pyrites occur as tiny grains aligned in an array within barite.			
Py-ii	Pyrite laminae.	−10.40 to 2.12	−1.19 to 1.46	−2.14 to 1.11
Py-iii	Individual grains or clusters associated with silica veinlets/beads in barite: within veinlet	−21.45 to −0.79	−1.38 to 1.50	−0.31 to 1.87
Py-iv	Individual grains or clusters associated with silica veinlets/beads in barite: on the wall of veinlet			
Py-v	Individual grains or clusters associated with silica veinlets/beads in barite: adjacent to both barite and chert			
Py-vi	Individual grains in barite with silica veinlets/beads	−18.99 to −1.54	−1.11 to 0.10	−0.16 to 1.20
Py-vii	Individual grains in chert with barite crystal fans	2.81 to 5.09	2.52 to 3.62	−2.92 to −2.63
Py-viii	Individual grains in silica-barite-carbonate vein in hydrothermally altered komatiitic basalt	1.67 to 2.39	−1.01 to −0.67	

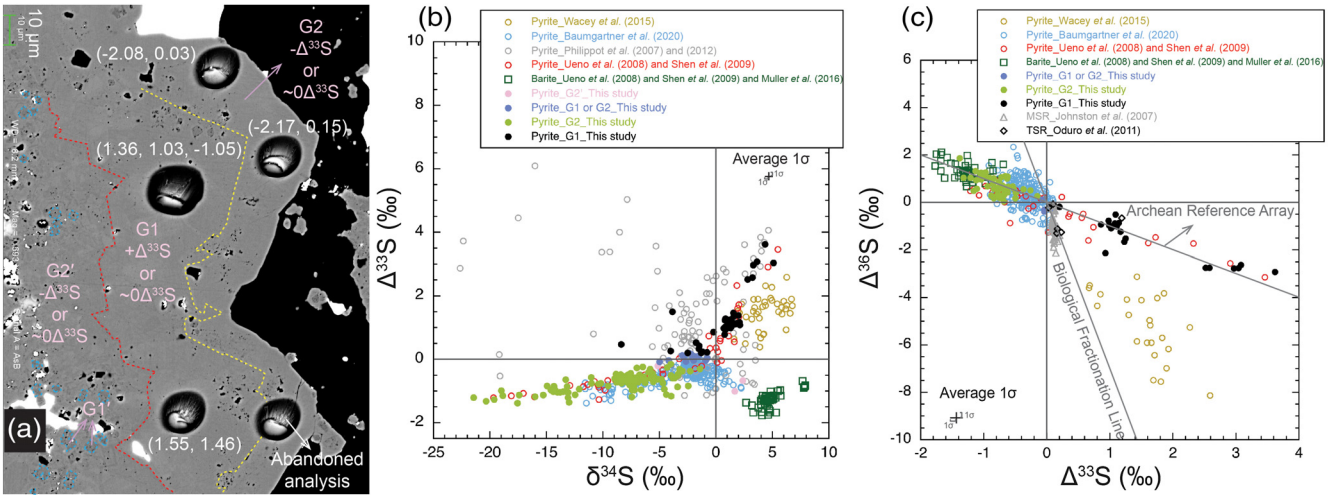

Figure 2 **(b)** $\delta^{34}S$-$\Delta^{33}S$ and **(c)** $\Delta^{33}S$-$\Delta^{36}S$ plots for G1, G2, G2′ pyrites, with **(a)** BSE image of a Py-ii showing four generations. Archaean Reference Array: $\Delta^{36}S \approx -\Delta^{33}S$ (Farquhar *et al.*, 2001); Biological Fractionation Line: $\Delta^{36}S \approx -7\Delta^{33}S$ (Ono *et al.*, 2006). $1\sigma = [(SE)^2 + (SD)^2]^{0.5}$, where SE is standard error of the analysis, and SD is standard deviation of Ruttan pyrite in the associated session.

(G2′) are partly oscillatory zoned and porous, and these have been measured by Baumgartner *et al.* (2020) and are mostly $\Delta^{33}S$-negative. One Py-ii (Fig. S-3d) has a $\Delta^{33}S$-negative core (oscillatory zoned) and $\Delta^{33}S$-positive rim, confirming G2′ precedes G1. Collectively, four generations are recorded in core-rim textured pyrites: $\Delta^{33}S$-positive G1′, $\Delta^{33}S$-negative G2′ (Baumgartner *et al.*, 2020), $\Delta^{33}S$-positive G1 and $\Delta^{33}S$-negative G2 (this study). The multiple generations of pyrites in the same sample can be attributed to multiple pulses of hydrothermal fluids, with the later generation overgrown on the earlier generation.

The pyrites with no internal texture (Py-ii to vi) have the same petrography as the core-rim textured counterparts, and show similar multiple sulfur isotope systematics to the cores and rims, thus the homogeneous pyrites (Py-ii to vi) are also categorised into the four generations based on $\Delta^{33}S$ and internal texture. The homogeneous Py-ii to vi lack the characteristic textures of G1′ and G2′, thus are all classified to G1 and G2. $\Delta^{33}S$-positive Py-vii are Ni-free and not porous, distinct from G1′ while similar to G1. The negative $\Delta^{33}S$ and positive $\delta^{34}S$ of Py-viii are similar to some G2′.

Photochemical reactions of gaseous sulfur species have been widely proposed to produce S-MIF, and the products are $\Delta^{33}S$-positive elemental sulfur and $\Delta^{33}S$-negative sulfate (Ono, 2017 and references therein). $\Delta^{33}S$-positive G1 and $\Delta^{33}S$-negative barites yield a line of $\Delta^{36}S = -0.98\Delta^{33}S + 0.05$ (Fig. S-10a). The slope is close to that for products of SO_2 photolysis under 193 nm UV (Farquhar *et al.*, 2001). Thus the photochemical products sulfate and elemental sulfur are likely to have been mostly sequestered in barites and G1 pyrites *via* reactions with Ba^{2+}-rich fluids and Fe^{2+}-, S^{2-}-rich fluids, respectively, with the magnitudes diluted by magmatic and/or $\Delta^{33}S$-opposite sign sulfur species in the atmosphere/water mass (detailed explanation in SI).

G1 yield a line of $\Delta^{36}S = -0.86\Delta^{33}S - 0.20$ (Fig. S-10b) close to the Archean Reference Array (ARA). Some G1 show slight deviations from ARA, both upwards and downwards (one analysis exhibits a downward offset of >1 ‰), suggesting possible microbial elemental sulfur disproportionation or sulfate reduction, respectively (Johnston *et al.*, 2007). However, neither is likely since microbial activities prefer ^{32}S over ^{34}S (*i.e.* negative $\delta^{34}S$) while G1 have positive $\delta^{34}S$.

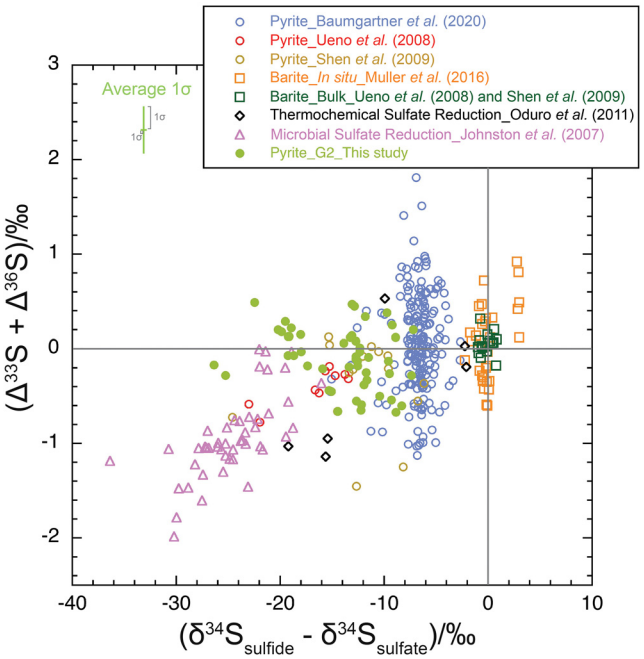

Figure 3 $(\delta^{34}S_{sulfide} - \delta^{34}S_{sulfate}) - (\Delta^{33}S + \Delta^{36}S)$ plot for G2, along with the initial sulfates, MSR and TSR. A $\delta^{34}S_{sulfate}$ value of 4.91 ‰ (the mean of Dresser barites) was used. Error bar 1σ of $(\delta^{34}S_{sulfide} - \delta^{34}S_{sulfate})$ is that of $\delta^{34}S_{sulfide}$ (G2), and 1σ of $(\Delta^{33}S + \Delta^{36}S)$ is $(\sigma_{\Delta 33S}^2 + \sigma_{\Delta 36S}^2)^{0.5}$.

G2 are most likely formed *via* the sulfide pathway, with S^{2-} derived from sulfate reduction. In addition to the sulfate in fluids and water mass, barite is also a possible sulfate source. G2 are closely associated with barites (*e.g.*, G2 occur within barites, in the silica veinlets of barites, or contain barite residue), and have similar $\Delta^{33}S$ despite smaller magnitudes. The solubility of barite can be increased by NaCl (Shi *et al.*, 2012) and silica (Cui *et al.*, 2019) that are present in the Dresser hydrothermal fluids (Harris *et al.*, 2009). Therefore, G2 can be derived from barite reduction, with Fe^{2+} and reductants brought in by hydrothermal fluids penetrated into barites as indicated by the widespread silica veinlets in barites. $\Delta^{33}S$ of G2 can have been diluted by (1) the involvement of magmatic $H_2S/HS^-/S^{2-}$ during pyrite formation *via* the sulfide pathway as indicated by the positive correlation between negative $\delta^{34}S$ and $\Delta^{33}S$ (Fig. 2b), and (2) the positive $\Delta^{33}S$ induced by sulfate reduction (thermochemical sulfate reduction, TSR; Oduro *et al.*, 2011; MSR, Johnston *et al.*, 2007).

The essential effects of MSR are the depletions in ^{34}S and downward shifts in $\Delta^{36}S/\Delta^{33}S$ (*i.e.* lower $(\Delta^{33}S + \Delta^{36}S)$[2] values) relative to the initial sulfate (Johnston *et al.*, 2007). Previous bulk analyses prefer MSR based on such signatures (Ueno *et al.*, 2008; Shen *et al.*, 2009). Admittedly, some G2 show negative $(\Delta^{33}S + \Delta^{36}S)$ (−0.03 to −0.67 ‰) and $\delta^{34}S$ fractionation of −7 to −26 ‰ from sulfate (the composition of sulfate is represented by that of barite), with portions plotted within the MSR area defined by culture experiments with sulfate reducers (2–36 °C; Figs. 2c, 3). However, the negative $(\Delta^{33}S + \Delta^{36}S)$ of the MSR area are relative to $(\Delta^{33}S + \Delta^{36}S)$ of 0 for initial sulfate. Bulk barite data are homogeneous with a restricted range of $(\Delta^{33}S + \Delta^{36}S)$ near 0 (Ueno *et al.*, 2008; Shen *et al.*, 2009), while *in situ* analyses results are variable with $(\Delta^{33}S + \Delta^{36}S)$ ranging from −0.60 to 0.92 ‰ (Muller *et al.*, 2016; Fig. 3). The $(\Delta^{33}S + \Delta^{36}S)$ range of G2 is similar to that of barites (*in situ* data, Fig. 3), and no significant downward shifts of G2 relative to initial barite are observed. Additionally, barites and G2 pyrites yield a line of $\Delta^{36}S = -0.99\Delta^{33}S - 0.02$ close to ARA while distinct from the Biological Fractionation Line (BFL; Fig. S-10c). Therefore, MSR signal in G2 is weak, although we do not exclude its presence because two data points of Shen *et al.* (2009) show negative $(\Delta^{33}S + \Delta^{36}S)$ even relative to the lowest $(\Delta^{33}S + \Delta^{36}S)$ value of *in situ* barite data.

Furthermore, some G2 show positive $(\Delta^{33}S + \Delta^{36}S)$ with larger magnitudes of positive shifts in $\Delta^{33}S$ than negative shifts in $\Delta^{36}S$, which has not been observed in MSR but has been discovered in TSR (Figs. 2c, 3). TSR can induce positive and negative $(\Delta^{33}S + \Delta^{36}S)$ depending on reductant and temperature (Oduro *et al.*, 2011), in addition to significant depletions in $\delta^{34}S$ relative to initial sulfate (Ohmoto and Goldhaber, 1997). Therefore, the S^{2-} of G2 can also be derived from TSR apart from MSR. TSR could be in operation 3.49 Ga ago in the Dresser hydrothermal system. This is consistent with the highest temperature of 110 °C where sulfate reducers (discovered so far) can live (Jørgensen *et al.*, 1992) while the temperature of the hydrothermal fluids associated with the Dresser Formation ranges from 300 °C at depth to 120 °C near the palaeosurface (Harris *et al.*, 2009).

Conclusions

A combination of sodium hypochlorite etching, BSE imaging and multiple sulfur isotopes reveals two main generations of pyrites associated with the barites of the 3.49 Ga Dresser Formation: $\Delta^{33}S$-positive G1 and $\delta^{34}S$- and $\Delta^{33}S$-negative G2. Diluted sulfate and elemental sulfur produced by photochemical reactions were sequestered in barites and G1, respectively. The positive $\delta^{34}S$ of G1 indicates an abiological genesis. G2 were formed *via* the sulfide pathway, with the sulfur derived from magmatic H_2S and S^{2-} produced by thermochemical and possible microbial sulfate reduction.

Acknowledgements

We sincerely thank the Perth Core Library for approving the access to drill cores and publishing the results. This work was supported by the Australian Research Council DP140103393 to TRI. The constructive comments from Dr. Boswell Wing and two anonymous reviewers are sincerely appreciated, which have improved this manuscript significantly.

Editor: Karim Benzerara

Additional Information

Supplementary Information accompanies this letter at https://www.geochemicalperspectivesletters.org/article2113.

[2] $(\Delta^{33}S + \Delta^{36}S)$ is derived from $\Delta^{36}S \approx -\Delta^{33}S$ (ARA), *i.e.* $\Delta^{33}S + \Delta^{36}S$ is 0 for data on ARA, but positive and negative for data above and below ARA, respectively.

Cite this letter as: Liu, L., Ireland, T.R., Holden, P. (2021) SHRIMP 4-S isotope systematics of two pyrite generations in the 3.49 Ga Dresser Formation. *Geochem. Persp. Let.* 17, 45–49.

References

Baumgartner, R.J., Caruso, S., Fiorentini, M.L., Van Kranendonk, M.J., Martin, L., Jeon, H., Pagès, A., Wacey, D. (2020) Sulfidization of 3.48 billion-year-old stromatolites of the Dresser Formation, Pilbara Craton: Constraints from in-situ sulfur isotope analysis of pyrite. *Chemical Geology* 538, 119488.

Buick, R., Dunlop, J.S.R., Groves, D.I. (1981) Stromatolite recognition in ancient rocks: an appraisal of irregularly laminated structures in an Early Archaean chert-barite unit from North Pole, Western Australia. *Alcheringa* 5, 161–181.

Cui, H., Zhong, R., Xie, Y., Yuan, X., Liu, W., Brugger, J., Yu, C. (2019) Forming sulfate- and REE-rich fluids in the presence of quartz. *Geology* 48, 145–148.

Farquhar, J., Savarino, J., Airieau, S., Thiemens, M.H. (2001) Observation of wavelength-sensitive mass-independent sulfur isotope effects during SO_2 photolysis: Implications for the early atmosphere. *Journal of Geophysical Research* 106, 32829–32839.

Harris, A.C., White, N.C., McPhie, J., Bull, S.W., Line, M.A., Skrzeczynski, R., Mernagh, T.P., Tosdal, R.M. (2009) Early Archean Hot Springs above Epithermal Veins, North Pole, Western Australia: New Insights from Fluid Inclusion Microanalysis. *Economic Geology* 104, 793–814.

Johnston, D.T., Farquhar, J., Canfield, D.E. (2007) Sulfur isotope insights into microbial sulfate reduction: When microbes meet models. *Geochimica et Cosmochimica Acta* 71, 3929–3947.

Jørgensen, B.B., Isaksen, M.F., Jannasch, H.W. (1992) Bacterial Sulfate Reduction Above 100 °C in Deep-Sea Hydrothermal Vent Sediments. *Science* 258, 1756–1757.

Muller, É., Philippot, P., Rollion-Bard, C., Cartigny, P. (2016) Multiple sulfur-isotope signatures in Archean sulfates and their implications for the chemistry and dynamics of the early atmosphere. *Proceedings of the National Academy of Sciences* 113, 7432–7437.

Noffke, N., Christian, D., Wacey, D., Hazen, R.M. (2013) Microbially Induced Sedimentary Structures Recording an Ancient Ecosystem in the ca. 3.48 Billion-Year-Old Dresser Formation, Pilbara, Western Australia. *Astrobiology* 13, 1103–1124.

Oduro, H., Harms, B., Sintim, H.O., Kaufman, A.J., Cody, G., Farquhar, J. (2011) Evidence of magnetic isotope effects during thermochemical sulfate reduction. *Proceedings of the National Academy of Sciences* 108, 17635–17638.

Ohmoto, H., Goldhaber, M.B. (1997) Sulfur and carbon isotopes. In: Barnes, H.L. (Ed.) *Geochemistry of Hydrothermal Ore Deposits.* Wiley, New York, 517–611.

Ono, S. (2017) Photochemistry of Sulfur Dioxide and the Origin of Mass-Independent Isotope Fractionation in Earth's Atmosphere. *Annual Review of Earth and Planetary Sciences* 45, 301–329.

Ono, S., Wing, B., Johnston, D., Farquhar, J., Rumble, D. (2006) Mass-dependent fractionation of quadruple stable sulfur isotope system as a new tracer of sulfur biogeochemical cycles. *Geochimica et Cosmochimica Acta* 70, 2238–2252.

Philippot, P., Van Zuilen, M., Lepot, K., Thomazo, C., Farquhar, J., Van Kranendonk, M.J. (2007) Early Archaean Microorganisms Preferred Elemental Sulfur, Not Sulfate. *Science* 317, 1534–1537.

Philippot, P., van Zuilen, M., Rollion-Bard, C. (2012) Variations in atmospheric sulphur chemistry on early Earth linked to volcanic activity. *Nature Geoscience* 5, 668–674.

Rickard, D., Luther, G.W. (1997) Kinetics of pyrite formation by the H_2S oxidation of iron (II) monosulfide in aqueous solutions between 25 and 125 °C: The mechanism. *Geochimica et Cosmochimica Acta* 61, 135–147.

Shen, Y., Farquhar, J., Masterson, A., Kaufman, A.J., Buick, R. (2009) Evaluating the role of microbial sulfate reduction in the early Archean using quadruple isotope systematics. *Earth and Planetary Science Letters* 279, 383–391.

Shi, W., Kan, A.T., Fan, C., Tomson, M.B. (2012) Solubility of Barite up to 250 °C and 1500 bar in up to 6 m NaCl Solution. *Industrial and Engineering Chemistry Research* 51, 3119–3128.

Tessalina, S.G., Bourdon, B., Van Kranendonk, M., Birck, J.L., Philippot, P. (2010) Influence of Hadean crust evident in basalts and cherts from the Pilbara Craton. *Nature Geoscience* 3, 214–217.

Ueno, Y., Yamada, K., Yoshida, N., Maruyama, S., Isozaki, Y. (2006) Evidence from fluid inclusions for microbial methanogenesis in the early Archaean era. *Nature* 440, 516–519.

Ueno, Y., Ono, S., Rumble, D., Maruyama, S. (2008) Quadruple sulfur isotope analysis of ca. 3.5 Ga Dresser Formation: New evidence for microbial sulfate reduction in the early Archean. *Geochimica et Cosmochimica Acta* 72, 5675–5691.

Wacey, D., Noffke, N., Cliff, J., Barley, M.E., Farquhar, J. (2015) Micro-scale quadruple sulfur isotope analysis of pyrite from the ~3480 Ma Dresser Formation: New insights into sulfur cycling on the early Earth. *Precambrian Research* 258, 24–35.

Van Kranendonk, M.J., Philippot, P., Lepot, K., Bodorkos, S., Pirajno, F. (2008) Geological setting of Earth's oldest fossils in the ca. 3.5 Ga Dresser Formation, Pilbara Craton, Western Australia. *Precambrian Research* 167, 93–124.